Fracture Detection from Seismic P-wave azimuthal AVO analysis – application to Valhall LoFS data

Ganyuan Xia & Leon Thomsen
BP E&P Technology, Houston, Texas, USA

Olav Barkved
BP Norway, Stavanger, Norway

ABSTRACT: The P-wave reflection amplitude variation as a function of offset and azimuth reveals much about the anisotropic nature of the subsurface rocks. Stress in the fractured reservoir may be closely linked to the seismic anisotropy. We propose and implement a method that systematically examines the amplitude vs. offset and azimuth (AVOAz) behavior of CMP gathers to invert for the implied fracture orientations and density, without arbitrary procedures such as azimuthal sectoring. Standard statistical methods, applied in this context, give us confidence interval and acceptance criteria for our results. We applied the technique to the Valhall Life Of Field Seismic (LOFS) dataset and produced relevant attribute maps at the reservoir level. The results indicate a strong correlation with changes in stress state associated with production-induced compaction in a fractured reservoir.

1 INTRODUCTOIN

1.1 *Fracture, stress and anisotropy*

Open fractures provide natural pathways for hydrocarbon movement. For fractured reservoirs with low matrix permeability, detailed and accurate description of fractures is the key to improve the production rate by optimally placing production wells, and to increase the ultimate recovery factor by intelligently designing water flood wells. A static description of the fracture system is not sufficient as the well activity causes changes in local effective stress field, which, coupled with regional stress, preferentially opens and closes fractures.

Stress in fractured reservoirs is closely linked to seismic anisotropy. For formations with sub-vertically aligned fractures, seismic velocity changes with respect to the azimuth, in addition to any changes with depth. A comprehensive review on seismic anisotropy can be found at Helbig & Thomsen (2005). Seismic anisotropy expresses itself in both traveltime and reflection amplitude. Both shear-wave splitting (birefringence) and P-wave velocity azimuthal variation can be studied to provide constraints on anisotropy. Such a study will be inherently low resolution, as traveltime is a cumulative property. However, because velocity varies with azimuth, the vertical contrast in velocity which gives rise to the reflection coefficient also varies with azimuth. Study of the amplitude variation with offset and azimuth (AVOAz) will provide a high resolution constraint on seismic anisotropy.

1.2 *AVOAz*

A wealth of information about the subsurface fluid types and lithology can be gained by studying the seismic Amplitude Versus Offset (AVO) effect. For isotropic media, the reflection coefficient R as a function of incidence angle θ may be approximated by

$$\mathbf{R}(\theta) \approx \mathbf{B}_0 + \mathbf{B}_1 \sin^2\theta + \mathbf{B}_2 \sin^2\theta \tan^2\theta \tag{1}$$

where $\mathbf{B_0}$, $\mathbf{B_1}$, $\mathbf{B_2}$ are conventionally referred to as AVO intercept, gradient, and curvature, respectively. They may be expressed as linear combinations of the material contrasts across a simple interface (Aki & Richards, 1980):

$$\boldsymbol{B}_0 = \frac{1}{2}\left(\frac{\Delta \boldsymbol{V_p}}{\bar{\boldsymbol{V}}_{\boldsymbol{p}}} + \frac{\Delta \rho}{\bar{\rho}}\right) \tag{2}$$

$$\boldsymbol{B}_1 = \frac{1}{2}\left[\frac{\Delta \boldsymbol{V_p}}{\bar{\boldsymbol{V}}_{\boldsymbol{p}}} - \left(\frac{2\bar{\boldsymbol{V}}_{\boldsymbol{s}}}{\bar{\boldsymbol{V}}_{\boldsymbol{p}}}\right)^2 \frac{\Delta \mu}{\bar{\mu}}\right] \tag{3}$$

$$\boldsymbol{B}_2 = \frac{1}{2}\frac{\Delta \boldsymbol{V_p}}{\bar{\boldsymbol{V}}_{\boldsymbol{p}}} \tag{4}$$

where $\mathbf{\Delta V_p}$, $\Delta\mu$ and $\Delta\rho$ are the changes (across the interface) in compressional wave velocity, shear modulus, and density, and the over-bars indicate averages across the interface. For small angles of incidence, the curvature term may be ignored.

Seismic amplitude as a function of incidence angle may be fitted in the least-squares sense to obtain estimates on the contrast parameters. The inversion, in the form of weighted stacks, tells us a great deal about the kind of rocks and fluids in rocks. Such an analysis makes the assumption of small angle of incidence, small contrasts in elastic property and, equally importantly, isotropy.

Subsurface rocks are in general anisotropic. Processes of sediment deposition in the vertical direction and preferential alignment of cracks give rise to intrinsic anisotropy; while the fine layering (compared to the seismic wavelengths) causes apparent anisotropy (Thomsen, 1986). Thomsen (1988) showed that polar anisotropy makes a first order effect on AVO.

If the fractures are vertically aligned, the reflection coefficient depends on both incidence angle and azimuth, because of the dependency of velocity on azimuth. The fracture density and orientation may be inferred by analyzing the amplitude variation with offset and azimuth (AVOAz) effect.

Currently there are two approaches to AVOAz analysis. One approach groups the input CMP gathers into common azimuth and offset bins. Conventional AVO analysis is performed with a few common azimuthal sectors, independently. The gradients from all sectors are them fitted with an ellipse. Binning to few discreet azimuths facilitates the use of standard 2D processing software. In addition, the power of stack helps by improving the signal-to-noise ratio within the nominal azimuthal sectors. However, it has major shortcomings. The binning procedure can lead to apparent anisotropy due to uneven sampling of source and receiver distribution. Also the procedure of mixing different azimuth and offset precludes meaningful error analysis. Furthermore the choice of sector seems arbitrary, and it tends to be richer in far offsets within each sector. Thomsen (priv comm., 1981), Holmes & Thomsen (2002), Hall & Kendall (2003), and Jenner (2003) proposed a different approach that takes into account the true acquisition geometry and fits the amplitude surface simultaneously. This is the approach that we choose in this paper. We describe the method of surface fitting first. Then we propose a methodology for estimating errors and introduce a model parameter rejection criteria based on standard statistics. We applied the method to the Valhall Life of Field Seismic (LOFS) 4D dataset where the dynamic reservoir dataset shows distinctive AVOAz effects.

2 METHOD

2.1 *AVOAz surface fitting*

For transverse anisotropic media with horizontal symmetry axis (HTI), the reflection coefficient depends on both incidence angle and azimuth. It has the same functional form as its isotropic counterpart

$$\mathbf{R}(\theta,\phi) \approx \mathbf{B}_0 + \mathbf{B}_1(\phi)\sin^2\theta + \mathbf{B}_2(\phi)\sin^2\theta\tan^2\theta \tag{5}$$

where $\mathbf{B_0}$, $\mathbf{B_1(\phi)}$, and $\mathbf{B_2(\phi)}$ are similarly defined as the AVO intercept, and azimuth-dependent gradient and curvature. They may be expressed in media contrast parameters also:

$$\boldsymbol{B}_0(\phi) = \frac{1}{2}\left(\frac{\Delta \boldsymbol{V}_{\boldsymbol{p}0}}{\overline{\boldsymbol{V}}_{\boldsymbol{p}0}} + \frac{\Delta\rho}{\overline{\rho}}\right) \tag{6}$$

$$\boldsymbol{B}_1(\phi) = \frac{1}{2}\left\{\frac{\Delta \boldsymbol{V}_{\boldsymbol{p}0}}{\overline{\boldsymbol{V}}_{\boldsymbol{p}0}} - \left(\frac{2\overline{\boldsymbol{V}}_{\boldsymbol{s}0}}{\overline{\boldsymbol{V}}_{\boldsymbol{p}0}}\right)^2 \frac{\Delta\mu_0}{\overline{\mu}_0} + \left[\Delta\delta^{\boldsymbol{v}} + \left(\frac{2\overline{\boldsymbol{V}}_{\boldsymbol{s}0}}{\overline{\boldsymbol{V}}_{\boldsymbol{p}0}}\right)^2 \Delta\gamma\right]\cos^2\phi\right\} \tag{7}$$

$$\boldsymbol{B}_2(\phi) = \frac{1}{2}\frac{\Delta \boldsymbol{V}_{\boldsymbol{p}0}}{\overline{\boldsymbol{V}}_{\boldsymbol{p}0}} + \Delta\varepsilon^{v}\cos^4\phi + \Delta\delta^{v}\sin^2\phi\cos^2\phi \tag{8}$$

where $\mathbf{V_{p0}}$, $\mathbf{V_{s0}}$, μ_0 are vertical compressional velocity, shear wave velocity and shear modulus (for shear polarization parallel to the symmetry planes), respectively; δ^v and ε^v are the modified Thomsen parameter (Ruger, 1998) and γ is the Thomsen parameter (Thomsen, 1986). Comparing Equations 6-8 with Equations 2-4, the similarity between these sets of equations is obvious, by design. For the HTI media, the gradient and curvature terms depend not only on the material property contrasts as in the isotropic case, but also on the azimuth. It is worth noting that the gradient term defines an ellipse with ϕ defined as the azimuth measured from the major axis of the anisotropy ellipse.

For small angles of incidence, we may ignore the third term in Equation 5. The small angle approximation leads to a more compact form for the P-wave reflectivity,

$$\boldsymbol{R}(\theta,\phi) \approx \boldsymbol{B}_0 + (\boldsymbol{G}_1 + \boldsymbol{G}_2\cos^2\phi)\sin^2\theta \tag{9}$$

Equation 9 clearly shows that the gradient term has a $\cos^2(\phi)$ dependency on azimuth with a period of π. However, the two-term fitting of amplitude on both incidence angle and azimuth is not straightforward, since ϕ is measured from the major axis of the anisotropic ellipse, which is unknown in general. Following a similar derivation due to Grechka & Tsvankin (1998) on elliptical NMO velocity fitting, Jenner (2002) used elementary trigonometric identities to recast the two-term AVOAz equation in a general form

$$\mathbf{R}(\theta,\varphi) \approx \mathbf{B}_0 + (\mathbf{W}_{11}\cos^2\varphi + \mathbf{W}_{12}\sin(2\varphi) + \mathbf{W}_{22}\sin^2\varphi)\sin^2\theta \tag{10}$$

where φ is the azimuth measured in a general coordinate system, and $\mathbf{W_{11}}$, $\mathbf{W_{12}}$ and $\mathbf{W_{22}}$ are the elements of a matrix $\mathbf{W}$. In fact, Ruger (1998) shows that this small-angle formulation (9-10) is valid beyond the HTI case of Equations (6-8), extending also to orthorhombic media with one axis vertical.

Equation 10 may be rewritten in matrix form, for the n data in an NMO-corrected, CMP gather of multiple offsets and azimuths, as:

$$\begin{pmatrix} \mathbf{R}_1 \\ \mathbf{R}_2 \\ \mathbf{R}_3 \\ \cdots \\ \mathbf{R}_\mathbf{n} \end{pmatrix} = \mathbf{A} \begin{pmatrix} \mathbf{B}_0 \\ \mathbf{W}_{11} \\ \mathbf{W}_{12} \\ \mathbf{W}_{22} \end{pmatrix} \tag{11}$$

where

$$\mathbf{A} = \begin{pmatrix} 1 & \cos^2\varphi_1 \sin^2\theta_1 & \sin(2\varphi_1)\sin^2\theta_1 & \sin^2\varphi_1 \sin^2\theta_1 \\ 1 & \cos^2\varphi_2 \sin^2\theta_2 & \sin(2\varphi_2)\sin^2\theta_2 & \sin^2\varphi_2 \sin^2\theta_2 \\ 1 & \cos^2\varphi_3 \sin^2\theta_3 & \sin(2\varphi_3)\sin^2\theta_3 & \sin^2\varphi_3 \sin^2\theta_3 \\ \cdots & \cdots & \cdots & \cdots \\ 1 & \cos^2\varphi_\mathbf{n} \sin^2\theta_\mathbf{n} & \sin(2\varphi_\mathbf{n})\sin^2\theta_\mathbf{n} & \sin^2\varphi_\mathbf{n} \sin^2\theta_\mathbf{n} \end{pmatrix} \tag{12}$$

Each datum may be the amplitude at a common time-sample, or the average amplitude over a common time-window.

Equations 11-12 represent a linear system which can be solved in the conventional least-squares fashion:

$$\begin{pmatrix} \mathbf{B}_0 \\ \mathbf{W}_{11} \\ \mathbf{W}_{12} \\ \mathbf{W}_{22} \end{pmatrix} = (\mathbf{A}^\mathbf{T}\mathbf{A})^{-1}\mathbf{A}^\mathbf{T} \begin{pmatrix} \mathbf{R}_1 \\ \mathbf{R}_2 \\ \mathbf{R}_3 \\ \cdots \\ \mathbf{R}_\mathbf{n} \end{pmatrix} \tag{13}$$

The two eigenvectors of the matrix **W** point in the two directions of the major and minor axes of the AVO gradient ellipse; the eigenvalues of **W** yield the lengths of the minor and major axis. In terms of the elements $\mathbf{W_{ij}}$ which are the direct solution of (13), the angle of the major axis, and the eigenvalues are:

$$\varphi_0 = \tan^{-1}\left[\frac{\mathbf{W}_{22} - \mathbf{W}_{11} + \sqrt{(\mathbf{W}_{22} - \mathbf{W}_{11})^2 + 4\mathbf{W}_{12}^{\;2}}}{2\mathbf{W}_{12}}\right] \tag{14}$$

$$\mathbf{G}_1 = \frac{1}{2}\left[\mathbf{W}_{22} + \mathbf{W}_{11} - \sqrt{(\mathbf{W}_{22} - \mathbf{W}_{11})^2 + 4\mathbf{W}_{12}^{\;2}}\right] \tag{15}$$

$$\mathbf{G}_2 = \sqrt{(\mathbf{W}_{22} - \mathbf{W}_{11})^2 + 4\mathbf{W}_{12}^{\;2}} \tag{16}$$

2.2 *Error analysis*

For a linear system such as equation 10, error estimation for model parameters may be derived from the model covariance,

$$\mathbf{C}_\mathbf{m} = (\mathbf{A}^\mathbf{T}\mathbf{C}_\mathbf{d}^{\;-1}\mathbf{A})^{-1} \tag{17}$$

where $\mathbf{C_d}$ is the data covariance and A is defined in Equation 12. The square root of the diagonal elements of model covariance $\mathbf{C_m}$ yields the model estimation error.

Translating the error estimates of $\mathbf{W_{ij}}$ to anisotropic gradients G_1 and G_2 and rotation azimuth φ_0 is not trivial, because Equations 14-16 involve trigonometry and power functions. For variables with independent probability distributions, the error is propagated by the derivative chain rule. For a variable v as a function of independent variables x and y, the standard deviation of v may be expressed as (cf., eg., Beers, 1962):

$$\mathbf{S}_\mathbf{v} = \sqrt{\left(\frac{\partial\mathbf{v}}{\partial\mathbf{x}}\right)^2 \mathbf{S}_\mathbf{x}^{\;2} + \left(\frac{\partial\mathbf{v}}{\partial\mathbf{y}}\right)^2 \mathbf{S}_\mathbf{y}^{\;2}} \tag{18}$$

where S_x and S_y and S_v are the standard deviation of x, y and v, respectively. Following this rule, we obtain the expression for model estimation errors for G_1 and G_2 and φ_0:

$$\mathbf{S}_{\mathbf{G}_2} = \frac{\sqrt{\left|\mathbf{w}_{11} - \mathbf{w}_{22}\right|\sqrt{\mathbf{S}_{\mathbf{w}_{11}}^{\;2} + \mathbf{S}_{\mathbf{w}_{22}}^{\;2}} + 8\left|\mathbf{w}_{12}\right|\mathbf{S}_{\mathbf{w}_{12}}}}{2\mathbf{G}_2} \tag{19}$$

$$\mathbf{S}_{\mathbf{G}_1} = \frac{\sqrt{\mathbf{S}_{\mathbf{w}_{11}}^{\;2} + \mathbf{S}_{\mathbf{w}_{22}}^{\;2} + \mathbf{S}_{\mathbf{G}_2}^{\;2}}}{2} \tag{20}$$

$$\mathbf{S}_{\varphi_0} = \tan(\varphi_0)\sqrt{\left(\frac{\mathbf{S}_{\mathbf{w}_{12}}}{\mathbf{w}_{12}}\right)^2 + \left(\frac{\mathbf{S}_{\mathbf{G}_1}}{\mathbf{w}_{11} + \mathbf{w}_{22} - \mathbf{w}_{\mathbf{G}_2}}\right)^2} \tag{21}$$

2.3 *Rejection criteria*

Sometimes the AVOAz surface does not fit well with the elliptical AVO gradient model, due to overwhelming noise in the data or lack of illumination at the target horizon, or simply absence of azimuthal anisotropy. We would like to mask out those solutions that do not agree with the model assumption. The "null-hypothesis" Student's t-test addresses the validity of the underlying model (cf eg, Mendenhall, 1971). According to the Student's t-test, if excluding a model parameter does not significantly decrease the quality of fit (of model to data), the model parameter should be "nullified". The statistical measure, the Student's t, is defined as

$$\mathbf{t}_\mathbf{y} = \frac{\mathbf{y}}{\mathbf{S}_\mathbf{y}} \tag{22}$$

where **y** can be $\mathbf{B_0}$, $\mathbf{G_1}$, $\mathbf{G_2}$ or $\boldsymbol{\varphi_0}$, and $\mathbf{S_y}$ is the corresponding standard deviation.

Note that the Student's t is a normalized quantity. Hence, it can be compared against the standard t-test table which lists the critical value of t as function of confidence interval and number of samples. For instance, the critical t value is 1.729 for 95% confidence and 20 samples. A calculated value of t larger than the critical t means that the "null hypothesis" (that the model parameter is null) may be rejected with confidence. In other words, the model should include the parameter with confidence.

3 APPLICATION OF AVOAZ TO VALHALL LOFS DATASETS

3.1 *Valhall field*

The Valhall field is an over-pressured, undersaturated Upper Cretaceous chalk reservoir located in the North Sea approximately 290 km offshore southern Norway in 69 m of water. The field is located in the southwestern corner of the Norwegian continental shelf (Figure 1). The field was discovered in 1975 and brought on stream in 1982. A total of 500 MMSTB has been produced, with remaining 500 MMSTB to be produced (Barkved et al. 2003).

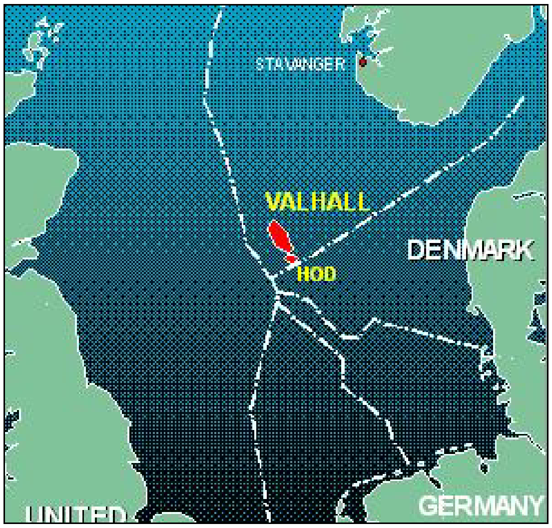

Figure 1. Location map of Valhall field.

Structurally, Valhall field is a double plunging NNW-SSE trending inversion anticline. Figure 2 shows a cross section of the field. The primary reservoir is the Tor formation with a secondary reservoir from a unit within the Hod Formation. The crestal part of the reservoir was naturally fractured. The reservoir is highly faulted, but the faulting does not extend well above the top of the hard chalk, nor far below the reservoir.

The reservoir is characterized as high porosity, low matrix permeability (<10md) chalk. However, production tests indicated an effective permeability an order of magnitude larger than that of the rock matrix (Ali & Alcock, 1994). Fractures were believed to be largely responsible for the unusually high permeability. The highly porous (>50%) and extremely soft chalk have resulted in rock compaction since the field began producing. Seabed subsidence (average rate of 50cm/yr) and well failures as the result of the rock compaction created large engineering challenges (Barkved, 2003). In additional compaction has also lead to dynamic reservoir properties, where initial fractures have closed upon pressure depletion while the new fractures may open.

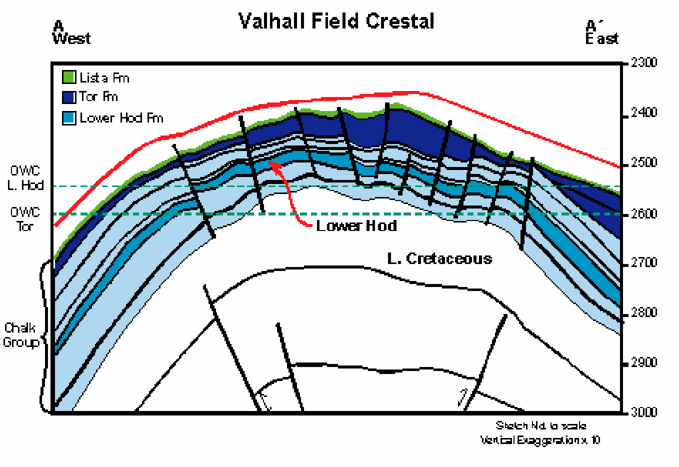

Figure 2. Cross section of the Valhall field.

The effective stress field changes as the result of rock compaction, coupled with the existing fractures lead to opening and closing of those fractures. If the opening and closing fractures are vertically aligned, AVOAz analysis in the time lapse sense can be used to give a high resolution picture of changes in anisotropy, from which inference can be made regarding the effective stress field and fracture system at the seismic scale.

3.2 *LOFS data*

Permanent Ocean Bottom Cables (OBC) were installed over the Valhall field during the summer of 2003, allowing for frequent time lapse seismic acquisition ("Life of Field Seismic (LOFS)", Barkved et al. 2004). To date six surveys have been acquired between October 2003 and October 2005. The LOFS datasets provide the basis for the reservoir management. Figure 3 shows the layout of the cables. The OBC consists of 2500 groups of 4C sensors covering 45 km^2. The inline sensor spacing is 50 m, and cross line 300 m. A regular shot patch (50 m x 50 m) is shot over the permanent cables, for each of the surveys.

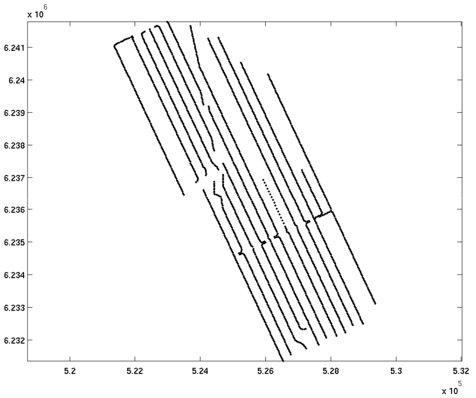

Figure 3. Layout of the OBC cables on the sea floor. The inline sensor spacing is 50 m, and the cables separation is 300 m. The hole in the middle is the location of the platform.

The LOFS acquisition design provides good offset and azimuth distribution, making AVOAz analysis feasible.

3.3 *Data processing*

All the LOFS datasets have been processed with the same processing flow to minimize the processing 4D effects. To maintain amplitude integrity, a minimal processing sequence is chosen. All the field acquisition geometry is preserved throughout the processing flow. No partial stacking is applied. Key steps are listed below in order:

- Vector fidelity correction
- PZ summation
- Noise removal
- 3D CMP sort
- NMO correction
- Amplitude balancing
- Trim statics correction
- AVOAz surface fitting
- Result QC

Since each LOFS survey records 4 components (X, Y, Z, and P), PZ summation is used to remove the water-layer ghosts. The bin size of 50 x 50 m was chosen to balance resolution with offset and azimuthal fold. A correlation-based trim-statics correction was applied to flatten events since this AVOAz analysis is carried out on the time sample basis. No migration was applied as the overall structure was relatively simple with gentle dips, and we wished to avoid the possible introduction of migration artifacts.

3.4 *A tale of two gathers*

(a) (b)

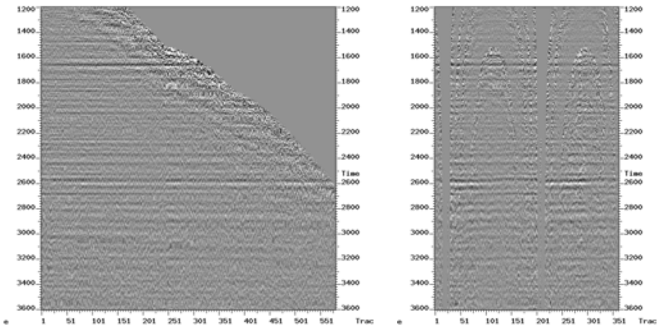

Figure 4. a)A typical 3D CMP gather sorted by increasing offset. The gather has been preprocessed and flattened. The top of the hard chalk is the bright reflection around 2600 ms. b) The same gather sorted by limited offset and azimuth. The THC reflection exhibits apparent azimuth variation with a period of π.

Figure 4a shows a typical 3D CMP gather, after trim statics correction, sorted by offset. Figure 4b shows the same gather sorted by azimuth for a limited offset range. The events are flattened and ready for the AVOAz surface fitting. The azimuthal variation of amplitude is clearly obvious to the eye in Figure 4(b), whereas it is masked in the conventional display of Figure 4(a). Of particular interest is the top hard chalk (THC) event, marked by the bright reflection at around 2600 ms two-way traveltime.

The source and receiver pairs of all the traces in this gather are displayed in a spider plot (Figure 5), showing good azimuthal and offset distribution.

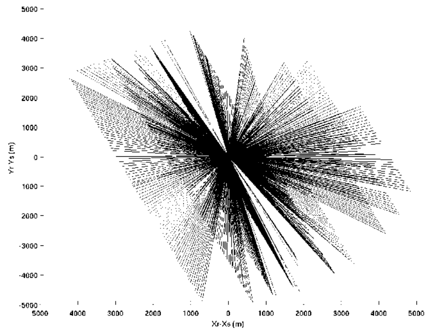

Figure 5. A spider plot of the source receiver pair for the CMP in Figure 4.

Some significant scatter is observed on the AVO gradient for this event, but there is a remarkable $\cos^2\varphi$ trend (Figure 6b), which is obscure when the gradient is (conventionally) sorted by offset (Figure 6a). Note that the anisotropic variation is in the same order of magnitude as the average; this is not a small effect. Despite the noise, the Student's t-test confirms that the anisotropic variation in the gradient should be accepted with confidence.

(a) (b)

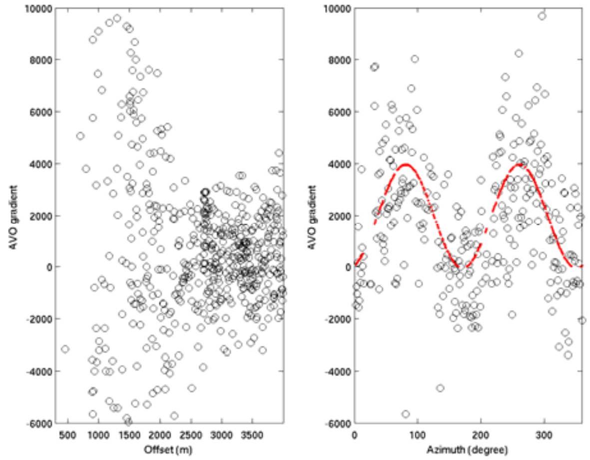

Figure 6. a) AVO gradient for the THC event. When sorted by offset as in the case of conventional AVO, the gradient appears to be "cloudy". b) When sorted by azimuth, a distinctive trend shows up. The trend is fitted in the least squares sense by an elliptical function, an indication of presence of anisotropy. The best-fit gradient is shown in dots, and the data gradient in circles.

The presence of a low velocity gas-charged shallow interval creates a "gas cloud" effect that masks the crestal part of the reservoir. This creates problems for P-wave based analysis – including AVOAz. A gather is picked from the "gas cloud" affected area and displayed in Figure 7. The THC event should be around 2640 ms for this location. The AVO gradient is scattered on the offset-sorted domain, and no distinctive trend can be identified on the azimuth sorted gather either (Figure 9), despite the good azimuthal and offset coverage (Figure 8). The Student's t-test, in this case, clearly indicates that the anisotropic gradient model should be rejected, agreeing with our intuition and observation.

(a) (b)

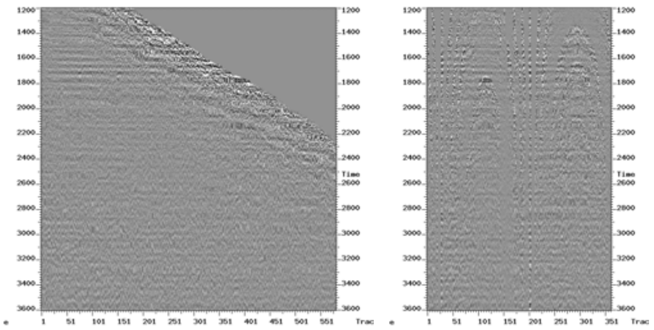

Figure 7. Gather selected from the "gas cloud" affected cretal structure. a) Sorted by increasing offset. The THC event around 2640 ms appears to be dim. b) The same gather sorted by azimuth for a limited offset range. No apparent azimuth variation is observed.

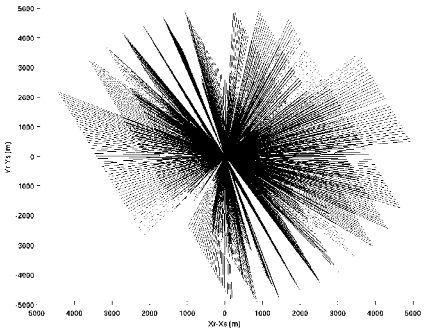

Figure 8. Spider plot showing the source and receiver pairs for the gather under the "gas cloud". Good azimuthal and offset distribution.

(a) (b)

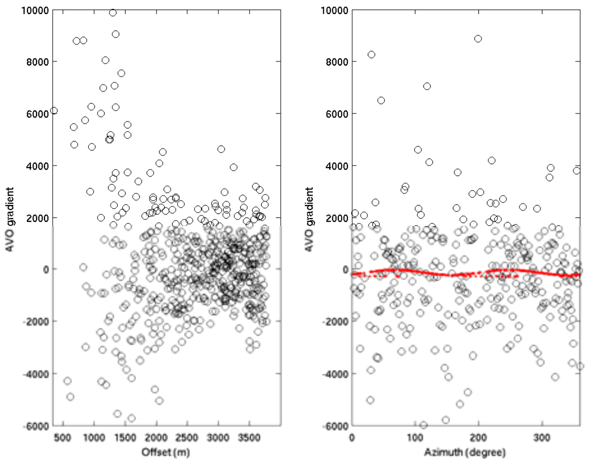

Figure 9. AVO gradient for the THC event from the gather under the "gas cloud". No apparent azimuthal variation is observed, regardless of the sorting order. The anisotropic gradient and orientation solutions are rejected base on the Student's t-test, due to poor data quality. a) Amplitude sorted by increasing offset. b) Amplitude sorted by azimuth. The best-fitting AVO gradient model is shown in solid dots, and data gradient in circles.

3.5 *Interpretation*

Two LOFS datasets (LOFS 1 & 2) were processed with this method, enabling 4D analysis. From the inverted parameter volume, various attributes are extracted along the THC horizon, and displayed in a map view for interpretation. Furthermore, the Student's t-test based reject criteria was used to mask off the results of low confidence.

Figure 10 shows a close-up view of the magnitude and orientation of the AVOAz effect. The colour intensity indicates the normalized anisotropic gradient, defined by the difference between the major and minor axes of the ellipse divided by the root-mean-square average of the two axes. The length and slope of the line segments represent the magnitude and orientation of the normalized anisotropic gradient, respectively.

The patchy appearance of the map is the result of applying the rejection criteria. We found this to be useful in aiding interpretation, because the interpreters will not be distracted by unnecessary details which the data do not support. The Student's t can be used as an opacity dial for visualization in real time.

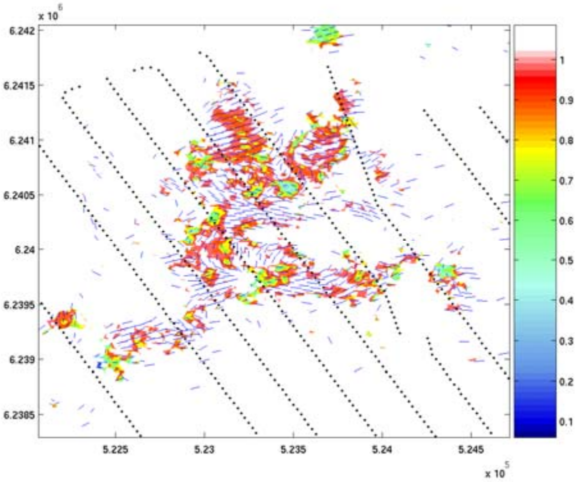

Figure 10. Implied fracture density and orientation for LOFS dataset 1 derived from the AVOAz analysis at the NW corner of the Valhall field with water injectors. The red dots are the 4C OBC sensors. The anisotropic gradient is normalized.

Note also that, within each patch, the fracture orientation shows a consistent pattern, not correlated with the acquisition direction. The orientations and azimuths are consistent within sub patches, although each bin is computed independently. The result agrees with the conclusion of Hall & Kendall (2003), based upon an older, sparser, and smaller OBC dataset, and extends those results across most of the field. The anomalies appear to correlate well with the major thickness of this area. The AVOAz analysis are done on un-migrated data, and in this area a likely pitfall is to track the event a leg too deep. The alternative interpretation for this is that the AVOAz character reflects opening of fracture in the layer below the reservoir, due to unloading effects associated with the depletion /compaction of the reservoir.

Figure 11 shows the normalized anisotropy gradient for the full survey area, overlaid with production well tracks. The anomalies seem to correlate with the well activity. We conclude that this AVOAz signature is a measure of azimuthal variation in physical rock properties at the reservoir level, accumulated over time, caused by well activity in the presence of subsurface stress. Hence, we call the resulting attribute maps the density and orientation of "implied fractures".

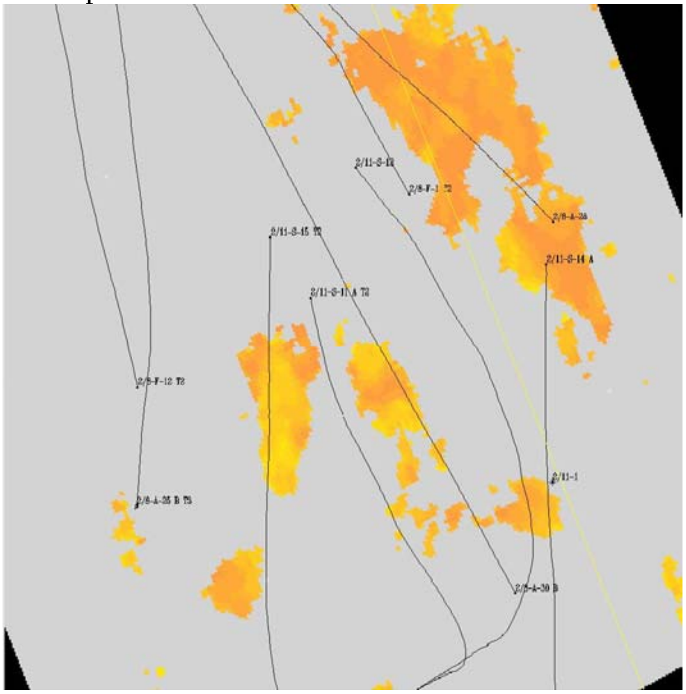

Figure 11. LOFS dataset 1. Well trajectories are posted on top of the fracture density map, showing good correlation with the well activity.

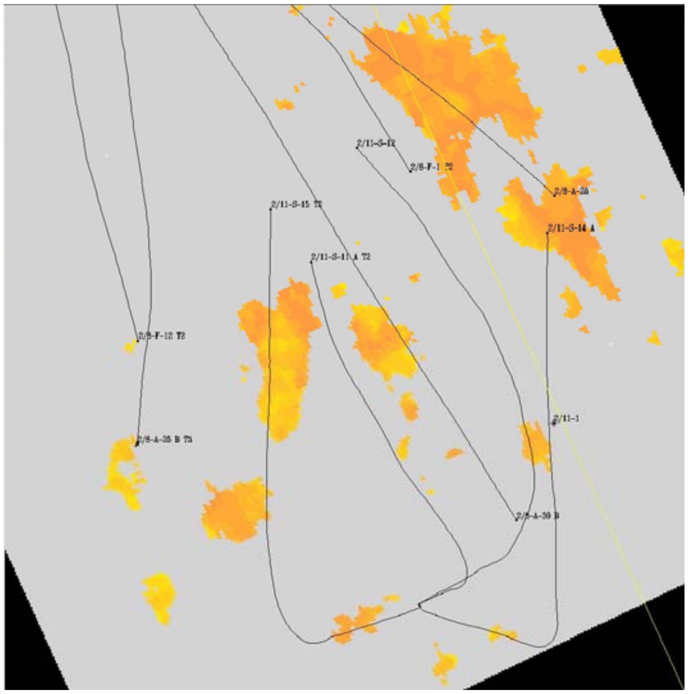

Figure 12. Same as Figure 11, but for LOFS 2.

The same procedure was applied to the LOFS dataset 2 acquired 3 months later. The static map from LOFS 2 resembles that of LOFS 1 (Figure 12).

The 4D difference map (Figure 13) (over an interval of 3 months) shows anomalies that seem to respond to the stress field change due to production. The AVOAz-anomalies as mapped in yellow appears on the fringe of the depleted area reflected by 4D anomalies defined from migrated stack volumes. In this area of the field there is less non-uniqueness of the interpretation, and the reference surface is at base reservoir. which is only 15 -25 m thick in most of this area.

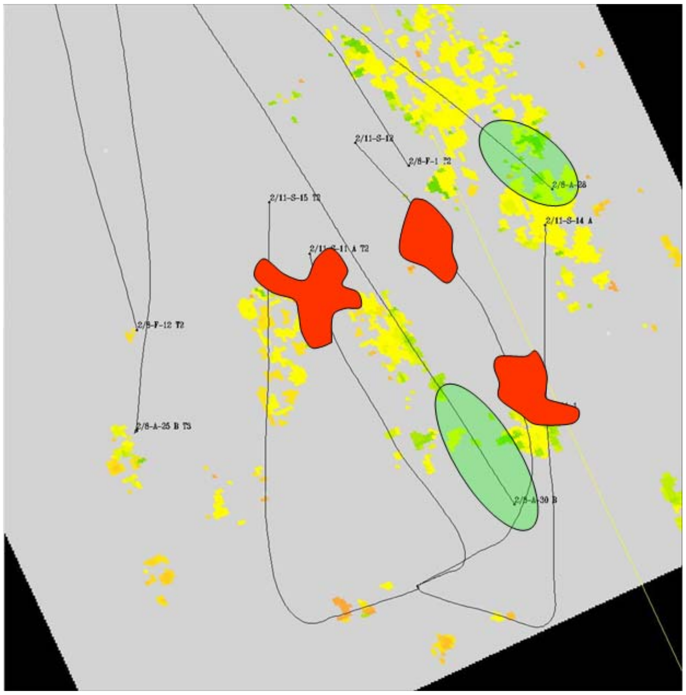

Figure 13. 4D difference map between LOFS 1 and 2. The red polygon enclosed areas reflect 4D amplitude anomalies mapped post-stack on the LoFS survey 2&3 , the green ellipse-highlighted areas are 4D amplitude anomalies from an older streamer 4D.

Production at the highly porous and extremely soft chalk reservoir leads to dynamic changes of properties and stress field. At the reservoir interval, compaction results in velocity and density increase; the unloading of the overburden causes sea bottom subsidence and decrease of velocity due to stress unloading. During injection, the pressure effects will be seen as an initial decrease in seismic velocities in the reservoir and an expected increase in velocities in the non-producing layers above and below the reservoir (Barkved 2005).

The changes in velocities affect both amplitude and traveltime. 4D time shifts and acoustic impedance changes have been extracted from the LOFS data (Barkved 2004). The acoustic impedance changes have been used in history matching (Kjelstadli et al. 2005). Including AVOAz attributes in the history match may provide additional constraint on the dynamic reservoir model.

Note that these 4D AVOAz changes are completely outside the logical framework of most 4D studies, which do not consider azimuthal changes at all. We report here time-lapse variation in azimuthal variation in offset variation of seismic amplitudes, properly acquired and processed, and show that such variation is in fact strong at Valhall.

4 CONCLUSIONS AND DISCUSSION

P-wave amplitude variation with offset and azimuth (AVOAz) provides key information about seismic anisotropy, from which inference can be made about fracture density and orientation. We propose and implement a surface fitting technique that analysis the AVOAz effect to provide high resolution estimates of implied fractures. The technique takes into account the actual acquisition geometry, a distinction from the binning approach. Statistical analysis applied in this context gives the confidence interval of model parameter estimates and also rejection criteria.

The technique was applied to Valhall LOFS datasets 1 and 2. Analysis of the implied fracture density and orientation at the top hard chalk horizon agrees with a previous study. The 4D difference map shows strong correlation with areas of expected change in the effective stress field, due to production and water injection at the fractured reservoir.

For Valhall field, where the reflection events are gently dipping, the locally 1D assumption is a good approximation. Prestack 3D CMP gathers can be used for AVOAz surface fitting directly. However, when the structures are complex, traces in the 3D CMP gather not longer come from the same subsurface reflector, invalidating the underlying 1D assumption for AVOAz analysis. Prestack depth migration is needed in this context to provide a local reflectivity as a function of local angle of incidence and azimuth that can feed into AVOAz analysis. Overburden effects can be treated by the migration as well.

ACKNOWLDEDGEMENTS

We thank BP and the Valhall partnership (BP Norge AS, Amerada Hess Norge AS, A/S Norske Shell and Total E&P Norge AS) for permission to publish this work. The results and opinions presented in this paper do not necessarily reflect the view of the Valhall partnership.

REFERENCE

Aki, K., & Richards, P.G. 1980. Quantitative seismology: Theory and methods: W.H. Freeman & Co.

Ali, N., & Alcock, T., 1994. Valhall field – The first 10 years, in North Sea oil and gas reservoirs III: Kluwer Academic Publishes, 25-40.

Barkved, O., Heave, P., Kjelstadl, R., Kleppan, T. & Kristiansen, T. 2003. Valhall field – still on plateau after 20 years of production, SPE 96317.

Barkved, O, Kommedal, J.H., & Thomsen, L., 2004, The role of multi-component seismic data in developing the Valhall Field, Norway. EAGE Expanded Abstract.

Barkved, O.I, and Kristiansen, T.G., 2005 Seismic time-lapse effects and stress changes: Examples from a compacting reservoir *The Leading Edge*, Volume 24, Issue 12, pp. 1244-1248

Beers, Y. 1962. Introduction to the theory of error, Addison-Wesley Publishing Company.

Grechka, G. & Tsvankin, I., 1998. 3-D description of normal moveout in anisotropic inhomogeneous media, *Geophysics*, 63, 1079-10092.

Hall, S.A.& Kendall, J-M. 2003. Fracture characterization at Valhall: Application of P-pave amplitude variation with offset and azimuth (AVOA) analysis to a 3D ocean-bottom data set, *Geophysics* 68(4): 1150-1160.

Helbig, K. & Thomsen L. 2005. 75-plus years of anisotropy in exploration and reservoir seismics: A historical review of concepts and methods, *Geophysics* 70(6): 9ND-23ND.

Holmes, G., & Thomsen., L., 2002. Seismic fracture detection at a Middle East offshore carbonate field, Soc. Petr. Eng. J., 78507.

Jenner, E 2002. Azimuthal AVO: Methodology and data examples, *The Leading Edge* 21(8):782-786.

Kjelstadli, R.M., Lane, S., Johnson, D., Barkved O., Buer, K. & Kristiansen, T. Quantitative history match of 4D seismic response and production data in the Valhall field, SPE 96317.

Mendenhall, W. 1971. Introduction to probability and statistics, *Duxbury Press*, Belmont, California.

Ruger, A. 1998. Variation of P-wave reflectivity with offset and azimuth in anisotropic media, *Geophysics* 63(3): 935-947.

Thomsen, L., 1986. Weak elastic anisotropy, *Geophysics* 51(10): 1954-1966.

Thomsen, L., 1988. Reflection seismology over azimuthally anisotropic media, *Geophysics* 53(3): 304-313.

Thomsen, L., 1995. Elastic anisotropy due to aligned cracks in porous rock: *Geophys. Prosp.*, 43, 805–829.